Supplementary Information

Selective area grown AlInGaN nanowire arrays with core-shell structures for photovoltaics on silicon

Renjie Wang, *[a] Shaobo Cheng,[b] Srinivas Vanka,[a,c] Gianluigi A Botton[b] and Zetian Mi*[a,c]

[a]Department of Electrical and Computer Engineering, McGill University, 3480 University Street, Montreal, QC H3A 0E9, Canada. Email: renjie.wang@mail.mcgill.ca, ztmi@umich.edu
[b]Department of Materials Science and Engineering, Canadian Centre for Electron Microscopy, McMaster University, 1280 Main Street West, Hamilton, ON L8S 4M1, Canada
[c]Department of Electrical Engineering and Computer Science, University of Michigan, 1301 Beal Avenue, Ann Arbor, Michigan 48109, USA

Table of Contents

Fig. S1: Bird’s-eye-view SEM image of selective-area grown (SAG) *p*-*i*-*n* AlInGaN nanowire (NW) array coated with polyimide resist.

Fig. S2: High-resolution high angle annular dark field scanning transmission electron microscopy (HAADF-STEM) image of interface between GaN:Si segment and Si substrate.

Table S1 and **Fig. S3:** Molecular beam epitaxy (MBE) parameters of thin AlN layer on Si tunnel-junction (TJ) solar cells (SCs) and the resulting photovoltaic (PV) characteristics.

Fig. S4 Photoelectrochemical (PEC) characterization of SAG *n*-GaN NW-array photoanodes on Si substrate.

Fig. S5: SAG AlInGaN NWs image.

Fig. S6: Photovoltaic characterizations of SAG *p*-*i*-*n* AlInGaN NW arrays grown with high Al incorporation.

Fig. S7: $\triangle V/\triangle I$ of SAG *p*-*i*-*n* AlInGaN NW arrays on *n*-Si substrate and SAG *n*-GaN/InGaN quantum dots/*p*-GaN on GaN/sapphire substrate.

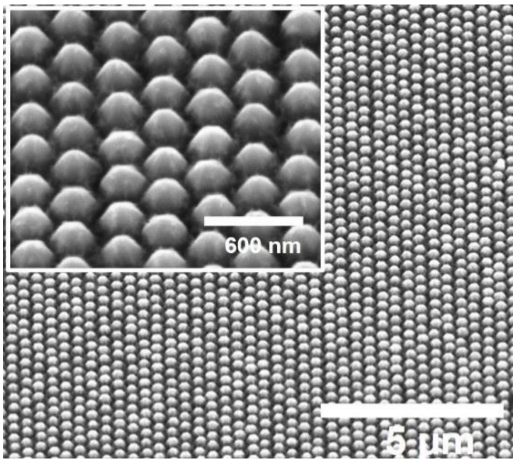

Fig. S1 SEM image of exposed GaN:Mg segments of NW array coated with polyimide resist. The inset is magnified image of exposed GaN:Mg array. Facility for Electron Microscopy Research, McGill University.

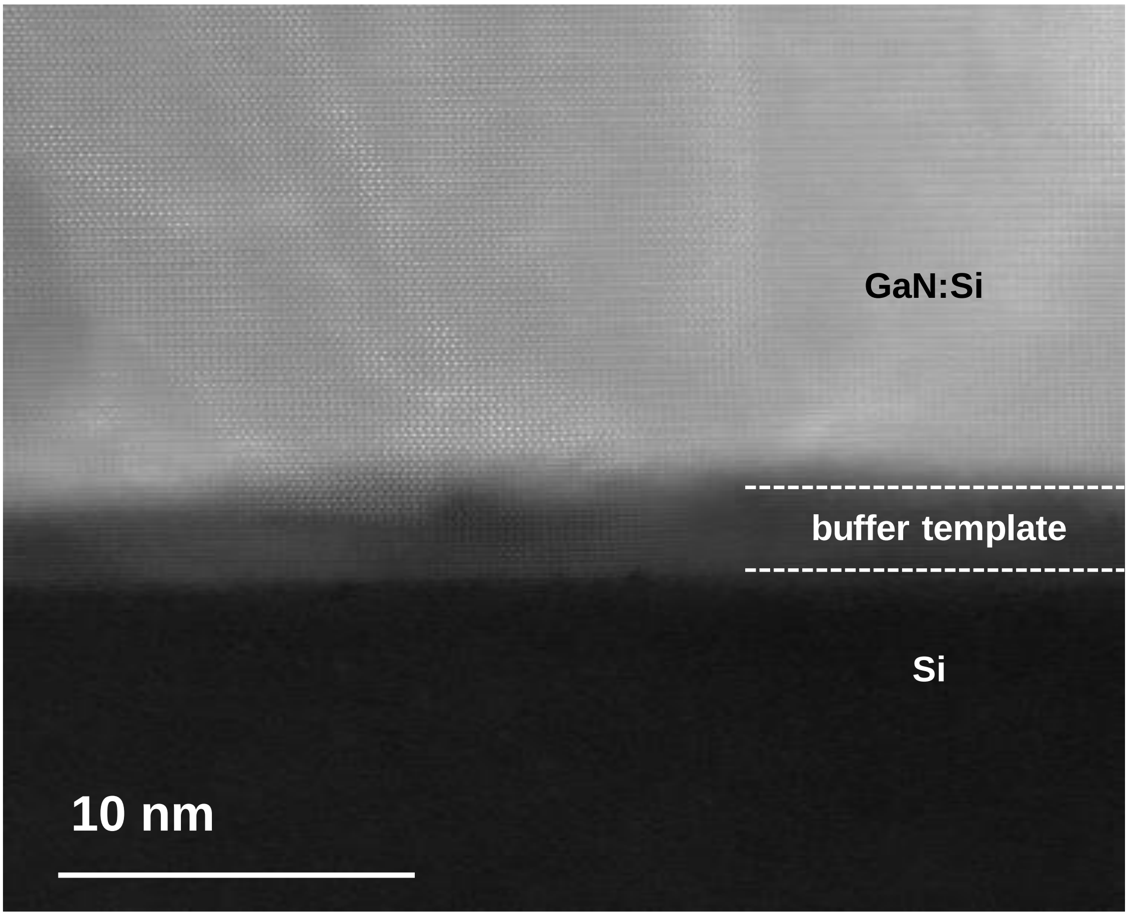

Fig. S2 The high-resolution HAADF-STEM image showing the interface between GaN:Si segment and Si substrate. In the thin AlN/GaN:Ge buffer layer, the presence of slightly different constrast may be due to the variations of composition and crystal orientations of buffer template. Canadian Centre for Electron Microscopy, McMaster University.

Table S1. MBE parameters of AlN layers on Si tunnel-junction SCs and the resulting PV characteristics.

Sample	Al *BEP* [$\times 10^{-8}$ Torr]	$T_{\mathrm{Substrate}}$ [°C]	J_{sc} [mA/cm^2]	V_{oc} [V]	η [%]	*FF* [%]
I	No AlN	No AlN	26.12	0.54	7.28	51.2
II	5.46	750	28.24	0.56	9.77	62.1
III	3.18	810	31.61	0.56	11.59	65.2

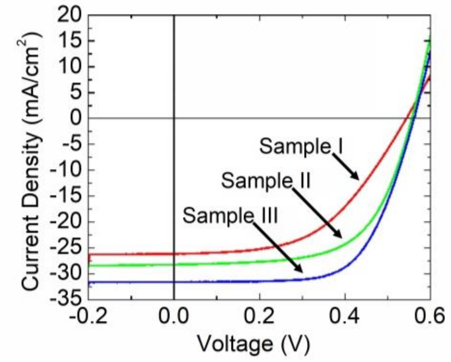

Fig. S3 Current density-voltage characteristics of Si SCs with a Si TJ. Sample I is as-fabricated Si TJ SCs, Sample II and Sample III were Si TJ SCs with thin AlN layer.

The effects of MBE-grown AlN layers on the PV characteristics of Si SCs with a p^+-Si/n-Si TJ were invesitgated. The preparation of Si SC wafer included spin coating of liquid boron (B) dopant precursor and liquid phosphorous (P) dopant precursor on the two surfaces of double-side-polished n-Si, and thermal annealing of the coated wafers for the conversions to p^+-Si and n^+-Si layers via thermal-diffusion doping process. Subsequently, liquid P-dopant precursor was spin coated on the surface of p^+-Si and underwent rapid thermal annealing to form few-nm-thick n-Si layer at the top of p^+-Si layer. The as-synthesized sample is denoted as Sample I (reference sample). The Si TJ-SC samples were loaded into RF PA MBE (Veeco, GEN II) system for the growth of thin AlN layer on the Si TJ (p^+-Si/n-Si) using various growth parameters shown in Table S1. To avoid SiN_x formation between Si and AlN layer, Al shutter were open prior to the excitation of N_2 plasma. Sample I, Sample II and Sample III were fabricated using the following procedures. Ti (20 nm)/Au (100 nm) metal was deposited on the n^+-Si layer as bottom metal contact by using e-beam evaporation. Ti (20 nm)/Au (100 nm) metal grid patterns were then deposited on TJ (p^+-Si/n-Si) as top metal contact by using standard photolithography and e-beam evaporation, followed by a rapid thermal annealing (RTA) at 550 °C in N_2 gas ambient for 1 min.

PV characteristics of Sample I, Sample II and Sample III under 100 mW/cm^2 illumination from an AM 1.5G solar simulator are summarized in Fig. S3. and in Table S1. Sample II and Sample III exhibit higher short-circuit current density (J_{sc}), conversion efficiency (η) and fill factor (*FF*) than Sample I. The increase in open-circuit voltage (V_{oc}) due to the addition of AlN layer is negligible, which is in the range of ~0.02 V. The improved J_{sc} and η are possibly due to AlN antireflection effect[1-3] instead of surface passivation effect. This study demonstrates the good electrical conductivity of AlN layer, and paves the way to integrate SAG III-nitride NWs with Si SCs for multijunction (Al)InGaN/Si integrated SCs and double-band (Al)InGaN/Si photoelectrochemical cells (PECs).

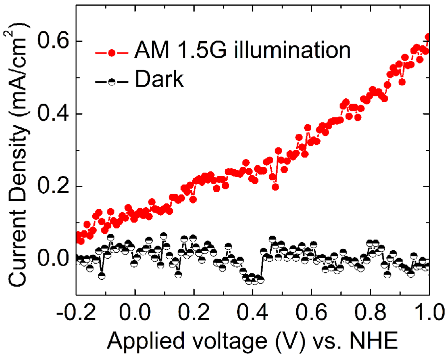

Fig. S4 Photoelectrochemical (PEC) characterization of *n*-GaN NW-array photoanodes selective-area grown on Si substrate. The variations of current density with applied voltage versus normal hydrogen electrode (NHE) for 0.014 cm^2 NW array in 1 M HBr solution under AM 1.5G illumination of 100 mW/cm^2 (red and solid symbol) and in dark environment (black and semi-hollow symbol).

The device preparation procedures and PEC characterization configurations can be found in literatures[4-7]. Both a thermopile (818P-100-55, Newport) and a photodiode sensor (818-ST2-UV/DB, Newport) with attenuator were used to calibrate the illumiantion intensity. Under AM 1.5G illumination of 100 mW/cm^2, the photo-current density (J_{ph}) reached 0.61 mA/cm^2 at 1.0 V versus normal hydrogen electrode (NHE).

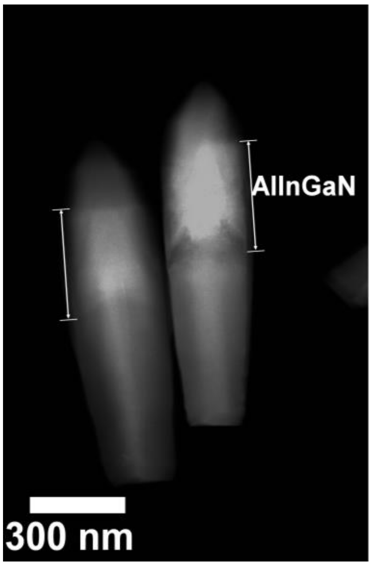

Fig. S5 An HAADF-STEM image of SAG GaN:Si/AlInGaN/GaN:Mg NWs. The labelled regions are AlInGaN segments showing In-rich AlInGaN core and AlGaN shell based on atomic-number contrast. Facility for Electron Microscopy Research, McGill University.

Figure S5 shows HAADF-STEM image of SAG AlInGaN NWs based on atomic-number contrast. Light element (Al) distribution presents dark constract while heavy element (In) distribution presents bright constrast. It is presented clearly from bottom to top that *n*-GaN, AlInGaN and *p*-GaN segments exhibit tapered and facted hexagonal structure with Ga polarity. AlInGaN segments presents brighter intensity at the center and darker intensity at the sidewall, indicating the formation of core-shell structure in SAG AlInGaN NWs. A core-shell structure has been reported from spontaneously grown AlInGaN NWs.[8]

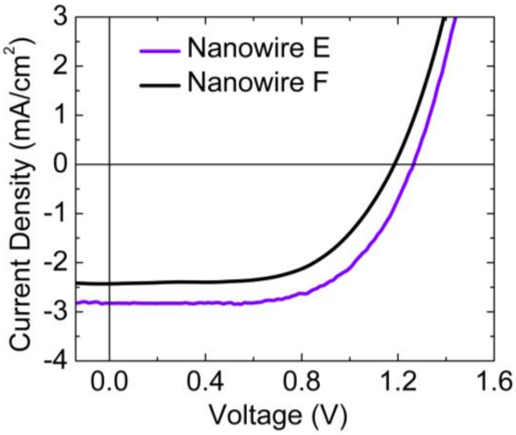

Fig. S6 Current density-voltage (*J*-*V*) output characteristics of two SAG AlInGaN NW SCs on Si substrates with high Al incorporation than that of NWs A, B, C and D. The samples differ in the MBE parameters of AlInGaN active segments.

The AlInGaN segments of NWs E and F have higher Al incorporation than those of NWs A, B, C and D. Compared to the small blueshift in peak wavelength of NWs A, B, C and D from 527.9 to 515.8 nm, the increased Al incorporation in NWs E and F lead to remarkable blueshift in PL emission from green emissions of NWs A, B, C and D to blue emission (465 nm) of NW E and deep-blue emission (432 nm) of NW F. As shown in Fig. S6, *J*-*V* output characteristics of NWs E and F exhibit lower J_{sc}, lower FF in the range of 0.594-0.615 and lower η in the range of 1.71-2.19%, compared to those of NW D SC.

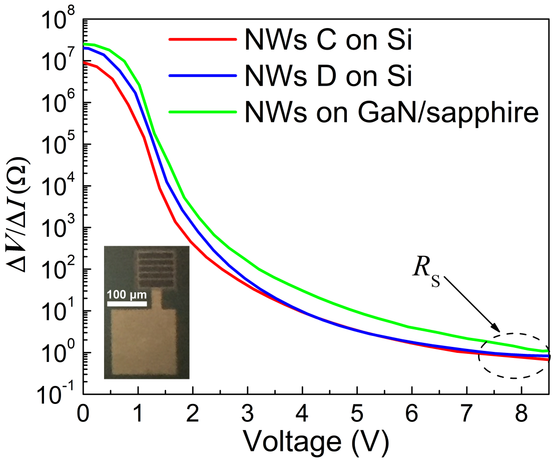

Fig. S7 $\triangle V/\triangle I$ of *n*-GaN/AlInGaN/*p*-GaN NW arrays (NWs C and NWs D) selective-area grown on *n*-Si substrate and *n*-GaN/InGaN quantum dots/*p*-GaN selective-area grown on GaN/sapphire substrate. $\triangle V/\triangle I$ is calculated based on the *I*-*V* characterisitcs of ~100×100 μm^2 SAG NW array under forward bias in the dark environment. The series resistances (R_s) are estimated by using similar methods in literatures[9-11]. The estimation of R_s is based on Equation 8. The inset is the image of ~100×100 μm^2 SAG NW array device (NWs C) on *n*-Si.

Reference

1. P. M. Kaminski, K. Bass and G. Claudio, *Phys. Status Solidi C*, 2011, **8**, 1311-1314.
2. G. Krugel, A. Sharma, W. Wolke, J. Rentsch and R. Preu, *Phys. Status Solidi RRL*, 2013, **7**, 457-460.
3. C. Wang, W. Cheng, P. Ma, R. Xia and X. Ling, *J. Mater. Chem. A*, 2017, **5**, 2852-2860.
4. S. Fan, B. AlOtaibi, S. Y. Woo, Y. Wang, G. A. Botton and Z. Mi, *Nano Lett.*, 2015, **15**, 2721-2726.
5. S. Fan, I. Shih and Z. Mi, *Adv. Energy Mater.*, 2017, **7**, 1600952.
6. S. Vanka, Y. Wang, P. Ghamari, S. Chu, A. Pandey, P. Bhattacharya, I. Shih and Z. Mi, *Solar RRL*, 2018, **2**.
7. S. Fan, S. Y. Woo, S. Vanka, G. A. Botton and Z. Mi, *APL Materials*, 2016, **4**.
8. R. Wang, X. Liu, I. Shih and Z. Mi, *Appl. Phys. Lett.*, 2015, **106**, 261104.
9. J.-K. Sheu, K.-H. Chang, S.-J. Tu, M.-L. Lee, C.-C. Yang, C.-K. Hsu and W.-C. Lai, *Opt. Express*, 2010, **18**, A562-A567.
10. M. Wolf and H. Rauschenbach, *Advanced Energy Conversion*, 1963, **3**, 455-479.
11. Y.-j. Liu, C.-c. Huang, T.-y. Chen, C.-s. Hsu, S.-y. Cheng, K.-w. Lin, J.-k. Liou and W.-c. Liu, *Progress in Natural Science: Materials International*, 2010, **20**, 70-75.